ARTICLE IN PRESS

npj 2D Materials and Applications

https://doi.org/10.1038/s41699-026-00706-0

Article in Press

# Hubbard dimer physics and the magnetostructural transition in the correlated cluster material $Nb_3Cl_8$

Received: 8 October 2025

Accepted: 1 May 2026

Cite this article as: Carta, A., Mlkvik, P., Grahlow, F. *et al.* Hubbard dimer physics and the magnetostructural transition in the correlated cluster material $Nb_3Cl_8$. *npj 2D Mater Appl* (2026). https://doi.org/10.1038/s41699-026-00706-0

Alberto Carta, Peter Mlkvik, Fabian Grahlow, Markus Ströbele, H.-Jürgen Meyer, Carl P. Romao, Nicola A. Spaldin & Claude Ederer

We are providing an unedited version of this manuscript to give early access to its findings. Before final publication, the manuscript will undergo further editing. Please note there may be errors present which affect the content, and all legal disclaimers apply.

If this paper is publishing under a Transparent Peer Review model then Peer Review reports will publish with the final article.

ARTICLE IN PRESS

© The Author(s) 2026. **Open Access** This article is licensed under a Creative Commons Attribution 4.0 International License, which permits use, sharing, adaptation, distribution and reproduction in any medium or format, as long as you give appropriate credit to the original author(s) and the source, provide a link to the Creative Commons licence, and indicate if changes were made. The images or other third party material in this article are included in the article's Creative Commons licence, unless indicated otherwise in a credit line to the material. If material is not included in the article's Creative Commons licence and your intended use is not permitted by statutory regulation or exceeds the permitted use, you will need to obtain permission directly from the copyright holder. To view a copy of this licence, visit http://creativecommons.org/licenses/by/4.0/.

ARTICLE IN PRESS

# Hubbard dimer physics and the magnetostructural transition in the correlated cluster material $Nb_3Cl_8$

Alberto Carta,[*,1,2,5] Peter Mlkvik,[*,2,5] Fabian Grahlow,[3] Markus Ströbele,[3] H.-Jürgen Meyer,[3] Carl P. Romao,[4] Nicola A. Spaldin,[2] and Claude Ederer[2]

[1] *PSI Center for Scientific Computing, Theory, and Data, PSI, 5232 Villigen, Switzerland*

[2] *Materials Theory, ETH Zürich, Wolfgang-Pauli-Strasse 27, 8093 Zürich, Switzerland*

[3] *Section for Solid State and Theoretical Inorganic Chemistry, Institute of Inorganic Chemistry, Eberhard-Karls-Universität Tübingen, Auf der Morgenstelle 18, 72076 Tübingen, Germany*

[4] *Department of Materials, Faculty of Nuclear Sciences and Physical Engineering, Czech Technical University in Prague, Trojanova 13, Prague 120 00, Czech Republic*

[5] *These authors contributed equally to this work.*

* E-mail: alberto.carta@psi.ch; peter.mlkvik@mat.ethz.ch

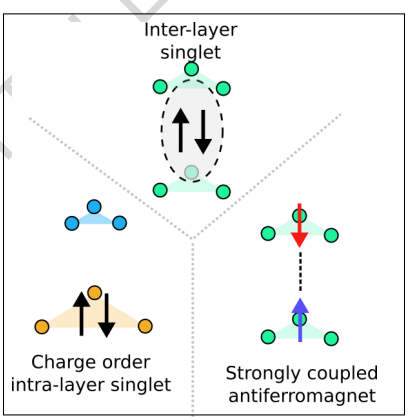
ARTICLE IN PRESS

ARTICLE IN PRESS

**Abstract**

We present a combined computational and experimental study of $Nb_3Cl_8$, a correlated layered material containing Nb trimers, through the lens of competing intra- and intercluster interactions. Different proposed explanations for its magnetostructural transition such as charge disproportionation, antiferromagnetic quenching, and interlayer singlet formation are investigated in light of the various reported low-temperature structures. Our findings rule out the previously proposed charge-disproportionation, suggest an intricate interplay between Mott physics and the formation of interlayer singlets, and also hint at a possible explanation of the observed intratrimer scissoring distortion. We suggest that the physics of $Nb_3Cl_8$ should be understood in the context of weakly coupled Hubbard dimers.

# TOC Graphic



ARTICLE IN PRESS

## Introduction

Cluster Mott insulators are strongly correlated materials for which the traditional definition of sites on which electrons interact [1] is extended to include clusters of atoms [2–7]. The interplay of charge and spin degrees of freedom, combined with the complexity introduced by the crystal field of the cluster, makes these materials an exciting playground to explore and engineer the physics of strongly correlated systems.

Among these, Kagome cluster magnets [8] have garnered considerable interest due to the interplay between magnetism and correlation effects. In this work, we focus on $Nb_3Cl_8$, part of the triniobium octahalide $Nb_3X_8$ ($X$ = Cl, Br, I) family. These compounds have recently been recognized as possible spin-liquid candidates [9, 10] and as obstructed-atomic-insulator candidates [11]; they exhibit thickness-dependent conductivity [12], display the anomalous valley Hall effect [13, 14], and have been showcased in Josephson diodes [15] and infrared sensors [16].

$Nb_3Cl_8$ is a layered 2D material consisting of $Nb_3Cl_{13}$ cluster units [circled in Fig. 1(a)] arranged in a breathing Kagome lattice [17–19] with short intratrimer bond distances of $d_{\text{Nb-Nb}} \cong 2.81$ Å (see SI [20], Supplementary Table 1). The nominal electronic filling of each trimer is 7 electrons and due to the octahedral coordination of the Nb ions in the cluster crystal field, the energy levels are split, leaving a lone electron in the $2a_1$ orbital [as shown in Fig. 1(d)]. In both the monolayer and bulk forms, these $a_1$ orbitals form narrow bands close to the Fermi level which are well separated from the rest of the electronic bands as shown in Fig. 1(e). Wannier functions corresponding to these $a_1$ states can be constructed as triangular molecular orbitals of mixed Nb-halogen character which are extended over the whole trimer [21] as seen in Fig. 1(f).

While the free-standing monolayer $Nb_3Cl_8$ has been characterized as a 2D Mott insulator both experimentally [22–24] and theoretically [9, 21, 22, 25, 26], the nature of the bulk material remains less explored. At high-temperature (HT), bulk $Nb_3Cl_8$ is found in the $\alpha$-phase with space group $P\bar{3}m1$, with two consecutive layers stacked in an AB-staggered pat-

ARTICLE IN PRESS

tern [12, 15, 19, 27–29]. The interlayer distance is $\sim 6.8\,\text{Å}$ while the intertrimer distance (distance between centers of adjacent $Nb_3$ trimers in the stacking direction) is $d_{\text{HT}} \cong 7.8\,\text{Å}$ [28] [Fig. 1(b), left].

As the temperature is lowered below $T_c \cong 100\,\text{K}$, the material remains insulating but undergoes a magnetostructural transition to the low-temperature (LT) $\beta$-phase which exhibits a significant change in the stacking pattern to an -AA'-BB'-CC'- arrangement [28, 30, 31]. This results in a "dimerization" of nearest-neighbor trimers along the stacking direction [Fig. 1(b), right] [28, 31]. The newly formed pairs' intertrimer distance decreases significantly to $d_{\text{LT}} \cong 6.1\,\text{Å}$ (see SI [20], Supplementary Table 1), and the calculated intertrimer hopping integral increases from $0.01\,\text{eV}$ to $t_{\text{LT}} \cong 0.13\,\text{eV}$ (see SI [20], Supplementary Table 2).

The space group of the LT $\beta$-$Nb_3Cl_8$ is still a matter of debate, with several different candidate structures proposed. Kim *et al.* [32], for instance, report $R\bar{3}m$ symmetry corresponding to the ideal version of this stacking, which has also been observed in other members of the extended $Nb_3X_8$ family: $Nb_3Cl_4Br_4$ [30], $Nb_3Br_8$ [33], and $Nb_3I_8$ [32]. In the literature, lower symmetry structures such as $R3$ [28, 34] and $C2/m$ [31] have also been proposed.

The different LT phases reported in the literature could plausibly be ascribed to differing experimental conditions used to synthesize and characterize $Nb_3Cl_8$ and related phases. The $R3$ and $C2/m$ phases have been observed using single crystal diffraction techniques [28, 31], which are generally highly sensitive to crystallographic symmetry, whereas $R\bar{3}m$ was assigned to the LT phase using a combination of experimental and theoretical vibrational spectroscopy [32], which is a less reliable method of determining the space group. $Nb_3Cl_4Br_4$ was also observed to adopt an $R\bar{3}m$ structure at low temperature using single crystal diffraction [30].

In all cases, the structural transition is accompanied by a significant drop in the magnetic susceptibility [28, 30, 31, 34], indicating a strong quenching of the local trimer moments. Several interpretations have been proposed to explain the observed drop in magnetic susceptibility. Haraguchi *et al.* [28, 34] report a "breathing" effect in the $Nb_3$ trimers,

with alternating layers of shorter and longer Nb-Nb bond lengths in the $R3$ structure from single-crystal X-ray diffraction (XRD). The authors propose charge disproportionation, $2[Nb_3]^7 \rightarrow [Nb_3]^8 + [Nb_3]^6$, leading to a formation of a singlet on the larger Nb trimers and causing a drop in the magnetic susceptibility [28].

When comparing $Nb_3Cl_8$ to other materials that exhibit singlet formation or charge disproportionation and subsequent structural distortions, several issues arise with the charge disproportionation model. Haraguchi *et al.* [28, 34] report bond lengths of $d_{\text{Nb1-Nb1}} = 2.801(3)$ Å and $d_{\text{Nb2-Nb2}} = 2.821(2)$ Å for the two inequivalent trimers, resulting in a notably small Nb-Nb bond-length difference of just 0.02 Å. We can compare these small distortions with other materials where metal-metal bonding is important. Vanadium dioxide ($VO_2$), for instance, is a material undergoing a similar paramagnetic-to-nonmagnetic transition associated with a formation of a V-V singlet state [35, 36]. $VO_2$ features a magnetostructural transition (coupled to a metal-insulator transition) contracting the original V-V bond by almost 10% or $\sim 0.3$ Å [37], roughly 15 times that observed in Ref. [28] for $Nb_3Cl_8$.

Moreover, using neutron diffraction, Sheckelton *et al.* [31] observe a different LT $Nb_3Cl_8$ structure which still exhibits the same magnetic-to-nonmagnetic transition, but has the $C2/m$ space group. This phase is characterized by an isosceles triangle geometry within the $Nb_3$ trimers leading to bond distances of $d_{\text{Nb1'-Nb2'}} = 2.86(2)$ Å and $d_{\text{Nb2'-Nb2'}} = 2.72(1)$ Å [31]. However, the authors ascribe the change of intratrimer distances to secondary effects and speculate that it is the stacking of the $\beta$ phase that drives a formation of singlets between different layers, causing the observed drop in susceptibility [31].

Computationally, due to the small bandwidth and thus the potential importance of local electron-electron interactions, $Nb_3Cl_8$ has largely been studied using a combination of density-functional theory (DFT) and dynamical mean-field theory (DMFT) [21, 22, 25, 38] or similar beyond-DFT methods [9, 39]. The bulk HT $\alpha$-$Nb_3Cl_8$ has been labeled as a cluster-Mott insulator with many similarities to the 2D precursor material [9, 21, 22, 25], consistent with the isolated local moments of the experimentally observed HT Curie-Weiss

susceptibility. For the LT $\beta$-$Nb_3Cl_8$ phase, most works agree on the important role of the increase in interlayer coupling [$t_{\mathrm{LT}}$ versus $t'_{\mathrm{LT}}$ in Fig. 1(c), see also SI [20], Supplementary Table 2], even though the specific proposals for the relevant physics vary.

By evaluating the role of an intratrimer Coulomb interaction correction $U_{tr}$, studies in bilayer LT $\beta$-$Nb_3Cl_8$ [22, 25] conclude that it is the competition between the interlayer hopping, $t_{\mathrm{LT}}$, and intratrimer Coulomb interaction that determines whether the system is an interlayer singlet insulator or a Mott insulator, with strong interlayer antiferromagnetic fluctuations. This conclusion has been bolstered by the studies on bulk systems from Grytsiuk, Aretz *et al.* [21, 38]. The same authors also report a change from a Mott insulating hypothetical $Nb_3F_8$ to a weakly correlated $Nb_3I_8$, due to the decreasing onsite Coulomb interaction $U_{tr}$ and the increasing interlayer hopping. Although the authors perform calculations of the experimentally observed $R3$ and the $C2/m$ structures [21], the origin and stability of the $\beta$ $Nb_3Cl_8$ low symmetry phases with respect to the $R\bar{3}m$ phase remains unclear.

In our work, we employ both DFT+$U$+$V$ [40] and DFT+DMFT [41] to assess and analyze the different mechanisms proposed for the observed magnetostructural transition using a basis of trimer-centered Wannier orbitals. The larger spatial extent of such molecular trimer orbitals in comparison to more localized atomic-like orbitals leads to a non-negligible intertrimer Coulomb repulsion $V_{tr}$ [38]. We hence consider both types of interactions, $U_{tr}$ and $V_{tr}$, and, in particular, focus on analyzing their influence on the physics of the bulk structure.

Our investigation of the different gap opening mechanism due to intra- and intercluster interactions in the LT $\beta$ phase shows a clear disagreement with the charge disproportionation picture [28, 34]. Instead, we obtain a continuous crossover between a Mott-insulating regime with strong antiferromagnetic intertrimer correlations and a band-insulator corresponding to the formation of intertrimer singlets [22, 25, 31, 38]. We conclude that the physics of LT $Nb_3Cl_8$ is well described within a picture of weakly coupled Hubbard dimers. Additionally, we also suggest a possible origin of the scissoring distortion reported in Sheckelton *et al.* [31]

resulting from atomic level interactions within the trimer. We corroborate our theoretical results with an experimental investigation of the structure and properties of $Nb_3Cl_8$ and $Nb_3Cl_4Br_4$, and suggest that synthesis conditions influence the LT phases of $Nb_3Br_{4-x}Cl_{4+x}$ materials.

# Results

## Stability of the $R3$ charge ordered phase

We begin by investigating the stability of the proposed trimer breathing mode coupling to charge order as described by Haraguchi *et al.* [28, 34].

To do so, we construct molecular trimer Wannier functions from the $2a_1$ bands that lie close to the Fermi level [Fig. 1(e)] following Ref. [21]. We then perform a series of DFT+$U$+$V$ calculations using these trimer orbitals as the basis, treating both the Coulomb interactions on one trimer ($U_{tr}$) and between adjacent trimers ($V_{tr}$). This is made possible by a recently developed extension of the QUANTUM ESPRESSO code [42].

The proposed breathing mode [see inset graphic in Fig. 2(c)] breaks the symmetry between the two trimers in the unit cell, leading to a difference in their onsite single-particle energies. Specifically, the energy of the long-edge trimer is lowered, while that of the short-edge trimer is raised.

In this section, we focus on spin unpolarized calculations, where the onsite occupation for spin up equals the onsite occupation for spin down, $n_{ii}^{\uparrow} = n_{ii}^{\downarrow} := n_{ii}$. The spin polarized case will be treated in the next section. In this case, the Hubbard contribution to the Kohn-Sham potential due to the onsite interaction parameter reads:

$$\Delta v_{ii}^{\sigma} = U_{\mathrm{tr}} \left( \frac{1}{2} - n_{ii} \right). \tag{1}$$

In the high-symmetry $R\bar{3}m$ structure, the two trimers are equivalent, leading to an onsite

ARTICLE IN PRESS

occupation of exactly $n_{ii} = 0.5$ for each one. Consequently, the potential correction from Eq. (1) is zero. A structural distortion, such as the trimer breathing mode that lowers the symmetry to $R3$, breaks this equivalence. This splitting of the trimer orbital energy levels creates a small initial occupation difference, $\Delta n$. The Hubbard $U$ term then acts to amplify this imbalance: for the more occupied trimer ($n_{ii} > 0.5$), $\Delta v_{ii}^{\sigma}$ is negative, favoring further filling, while for the less occupied one ($n_{ii} < 0.5$), $\Delta v_{ii}^{\sigma}$ is positive, promoting emptying. Following the charge disproportionation model proposed by Haraguchi *et al.* [28], a sufficiently strong Hubbard $U$ can be expected to drive this system towards a larger occupation difference, potentially approaching the limit of two electrons, thereby forming a singlet state on one trimer while completely emptying the other. However, our calculations reveal that this amplification effect is rather weak, as also manifested by the small onsite energy difference due to the trimer breathing distortion (see SI [20], Supplementary Fig. 1).

Our results are presented in Fig. 2(a, b) where we plot the occupation difference and the energy as a function of the trimer breathing mode amplitude which is defined as the edge difference between long-edge and short-edge trimers, for values around the calculated constrained random-phase approximation (cRPA) values [$(U_{\mathrm{tr}}, V_{\mathrm{tr}}) = (1.46, 0.38)\,\mathrm{eV}$, see SI [20], Supplementary Table 2]. We explicitly vary the trimerization distortion mode and calculate the energy separately at every step. We remark that the absolute value of the energy difference between calculations with different $U_{\mathrm{tr}}$ and $V_{\mathrm{tr}}$ is not physically meaningful, and it is only shown in Fig. 2(b) for visual clarity.

We find that for $(U_{\mathrm{tr}}, V_{\mathrm{tr}}) = (1.5, 0.0)\,\mathrm{eV}$, the reported $R3$ structure [28, 34] corresponds to an occupation difference of only 0.03 electrons [see vertical dashed line in Fig. 2(a)]. We observe that even at $U_{\mathrm{tr}} = 2.5\,\mathrm{eV}$ (60% higher than the computed cRPA value) and at a breathing mode amplitude of 0.4 Å (20 times the experimental value), the occupation difference remains smaller than 0.4 electrons. Furthermore, we observe that the energy minimum consistently occurs at zero breathing mode, which corresponds to the higher symmetry $R\bar{3}m$ structure [Fig. 2(b)].

ARTICLE IN PRESS

By examining the band structure at different breathing mode amplitudes [Fig. 2(c)], we observe minimal changes in the bands near the Fermi level as the breathing mode amplitude increases, and the material remains metallic. This finding is not consistent with the experimentally observed insulating behavior.

To investigate this point further we perform calculations where in addition to the $+U$ correction we include an intersite term $V_{\mathrm{tr}}$. The $+V$ correction essentially modifies the effective hopping between neighboring sites by adding an intersite potential [40]:

$$\Delta v_{ij}^{\sigma} = -V_{\mathrm{tr}} n_{ji}^{\sigma} \quad . \tag{2}$$

Here $n_{ji}^{\sigma}$ is the off-diagonal intertrimer component of the density matrix which is a measure of the intersite hybridization.

Upon including $V_{\mathrm{tr}}$ [light red and red lines in Fig. 2(a, b)], we observe a further suppression of the occupation difference between trimers. This is accompanied by an opening of a band gap [Fig. 2(d)], the nature of which will be discussed more in detail in the next section.

Consequently, based on our DFT+$U$+$V$ calculations, the charge-ordered phase accompanied by a trimer breathing mode as proposed by Haraguchi *et al.* [28] appears to be energetically unfavorable. We therefore rule out the charge disproportionation mechanism as explanation for the observed magnetic-nonmagnetic transition in $Nb_3Cl_8$.

## Origin of the quenched magnetism in the $R\bar{3}m$ phase

We now consider different possible explanations of the low susceptibility observed in $\beta$-$Nb_3Cl_8$. In this section, we study separately the effects of the interaction terms $U_{\mathrm{tr}}$ and $V_{\mathrm{tr}}$, allowing for spin-polarization in the system.

As previously mentioned, with no spin-polarization, one would expect the $+U$ correction to promote charge polarization in one of the trimer orbitals. In spin-polarized calculations instead, the $+U$ correction can favor the formation of an onsite magnetic moment on the

$Nb_3$ molecular orbital. This is because the potential shift $\Delta v_{ii}^{\sigma} = U_{\mathrm{tr}} \left(\frac{1}{2} - n_{ii}^{\sigma}\right)$ for site $i$ and spin $\sigma$, promotes either fully occupied or completely empty spin channels on each orbital. So, at strong $U$, one would expect for one trimer orbital one spin channel $\sigma$ to be completely occupied $n_{ii}^{\sigma} \sim 1$ and the opposite spin channel $\bar{\sigma}$ to be empty $n_{ii}^{\bar{\sigma}} \sim 0$, which corresponds to the formation of a local magnetic moment on the trimer.

In Fig. 3(a, b), we show the average onsite trimer moment $|n_{ii}^{\uparrow} - n_{ii}^{\downarrow}|$ and the magnitude of the off-diagonal occupation matrix element $n_{ij}^{\sigma}$, respectively, as a function of $U_{\mathrm{tr}}$ and $V_{\mathrm{tr}}$. In Fig. 3(c), we show the band structure for fixed $V_{\mathrm{tr}}$ and changing $U_{\mathrm{tr}}$.

Two competing tendencies emerge: a strong onsite Coulomb interaction $U_{\mathrm{tr}}$ favors the development of antiferromagnetically aligned local magnetic moments on the $Nb_3$ sites [Fig. 3(a)], suppressing any intersite bonding [$n_{ij}^{\sigma} \to 0$ in Fig. 3(b)].

This local moment formation leads to a band gap opening [Fig. 3(c)] and the strong antiferromagnetic correlations between adjacent trimers could be responsible for the suppression of the magnetic susceptibility [21]. We underline that we are not arguing for the presence of long-range antiferromagnetic order in the material. Rather, we argue that in the strong $U_{\mathrm{tr}}$ regime nearest neighboring trimer orbitals could show strong antiferromagnetic correlations, as schematically depicted in the inset in Fig. 3(c). Conversely, a dominant intersite Coulomb interaction $V_{\mathrm{tr}}$ promotes the formation of bonding-antibonding states between trimers ($n_{ij}^{\sigma} = 0.5$) [Fig. 3(b)] and also leads to the formation of a band gap [as was previously shown in Fig. 2(d)], which in this case is related to the large bonding-antibonding splitting. Since two electrons per dimer would then occupy the lower-lying bonding state, forming a nonmagnetic singlet [inset in Fig. 2(d)], this scenario would also be compatible with a drop in magnetic susceptibility.

Our cRPA calculations for the trimer molecular orbitals, in good agreement with the findings of Grytsiuk, Aretz *et al.* [21, 38], suggest that $Nb_3Cl_8$ lies closer to the strong $U_{\mathrm{tr}}$ regime.

To summarize, our calculations indicate that a change in stacking from $P\bar{3}m1$ to $R\bar{3}m$

ARTICLE IN PRESS

is sufficient to explain the low magnetic susceptibility observed in $\beta$-$Nb_3Cl_8$, without the need to introduce any further symmetry-lowering distortions, in agreement with previous works [21, 38].

## Dynamical effects in the $R\bar{3}m$ phase

So far, our treatment of the physics in $Nb_3Cl_8$ has been based on a static mean-field treatment of interaction effects, which highlights the crucial role of both onsite and intersite interactions, particularly within dimerized units of $Nb_3$ molecular orbitals. To move beyond this static mean-field approximation and capture dynamical effects, we now employ DFT + cluster DMFT, which has been shown to be a particularly viable approach for studying quantum singlet-like states [38, 43].

We construct a DMFT impurity problem for the $R\bar{3}m$ structure using a cluster of two neighboring molecular trimer orbitals, as first introduced in Aretz *et al.* [38], and explore the behavior of the system under a variety of interaction parameters, in particular exploring the nature of the insulating state.

This approach is well suited for systems like $Nb_3Cl_8$ due to the strong onsite and intersite interactions $U_{tr}$ and $V_{tr}$, a significant intertrimer hopping along the stacking direction ($t_{\mathrm{LT}} = 0.13\,\mathrm{eV}$ , see SI [20], Supplementary Table 2, and comparatively weaker hybridization between the dimerized cluster and the rest of the $Nb_3$ molecular orbitals in plane ($t_{\mathrm{LT}}^{\mathrm{in-plane}} = 0.02\,\mathrm{eV}$, see SI [20], Supplementary Table 1). These considerations allow us to draw significant analogies between the physics in the LT phase of the $Nb_3X_8$ family and the so-called *Hubbard dimer*, a model system consisting of two interacting sites with one orbital each.

For two electrons in the Hubbard dimer model (i.e., at half filling), the gap, $E_g$, in the excitation spectrum between the highest occupied and lowest unoccupied states of the Hubbard dimer, is dependent on the three parameters that define the model, the intersite

ARTICLE IN PRESS

hopping $t$, the onsite $U$ and the intersite $V$ interaction parameters [44]:

$$E_g = -2t + V + \sqrt{(U-V)^2 + 16t^2}. \tag{3}$$

In general the (unnormalized) ground state of such a model system $|\psi_0^{\text{dimer}}\rangle$ can be written as:

$$\begin{aligned} |\psi_0^{\text{dimer}}\rangle = A(|\uparrow,\downarrow\rangle - |\downarrow,\uparrow\rangle) \\ +(|\uparrow\downarrow,0\rangle + |0,\uparrow\downarrow\rangle), \end{aligned} \tag{4}$$

where $A = 4t/[\sqrt{(U-V)^2+16t^2} - (U-V)]$. Here, $|\uparrow,\downarrow\rangle$ corresponds to a state with an up-spin electron on the first and a down spin electron on the second site, whereas $|\uparrow\downarrow,0\rangle$ corresponds to double occupation of the first site, and analogous for the other states in Eq. (4).

For $U = V$, $A = 1$ the ground state can be described by a single Slater determinant expressed in the bonding-antibonding basis, and corresponds to the bonded state of two trimer sites. The opposite limit, $U \gg V$, $A \to \infty$, corresponds to the suppression of double occupancies and the maximally correlated state, the Heitler-London limit.

In Fig. 4(a-d), we depict the dependence of various properties of $\beta$-$Nb_3Cl_8$ on both $U_{\text{tr}}$ and $V_{\text{tr}}$. We show the band gap [Fig. 4(a)] obtained from the spectral function, and the quasiparticle weight [Fig. 4(b)] defined from the frequency dependence of the self-energy. In addition, we also show the off-diagonal occupation matrix element [Fig. 4(c)], and the probability of double occupancy on one of the $Nb_3$ molecular orbitals [Fig. 4(d)]. The latter is obtained from analyzing the probability of the various multiplet states occurring in the two site cluster, based on the statistics from the employed quantum Monte Carlo solver.

We obtain an insulating solution for any value of the tested $U_{\text{tr}}$ and $V_{\text{tr}}$ parameters, except in the vicinity of $U_{\text{tr}} = V_{\text{tr}} = 0$ [Fig. 4(a)], with the size of the band gap depending on both $U_{\text{tr}}$ and $V_{\text{tr}}$. At high $U_{\text{tr}}$ and small $V_{\text{tr}}$, the insulator exhibits hallmark features of

ARTICLE IN PRESS

a Mott state, such as a vanishing quasiparticle weight [Fig. 4(b)]. By increasing $V_{\mathrm{tr}}/U_{\mathrm{tr}}$, the quasiparticle weight rises, reaching $Z = 1$ at $U_{\mathrm{tr}} = V_{\mathrm{tr}}$, where the system is a band insulator. This is accompanied by a gradual increase in the off-diagonal occupation from $V_{\mathrm{tr}} = 0$ to the maximum 0.5 at $U_{\mathrm{tr}} = V_{\mathrm{tr}}$, with the double occupation probability changing in a similar way [Fig. 4(c, d)]. At small $V_{\mathrm{tr}}/U_{\mathrm{tr}}$, our results show a marked suppression of double occupancies highlighting the localization of a single electron per $Nb_3$ site. The multiplet analysis can also clarify the relative spin orientation of the $Nb_3$ sites. Even at small $V_{\mathrm{tr}}/U_{\mathrm{tr}}$, configurations with spins aligning in opposite directions between trimers have high probability, while configurations where spins point in the same direction on both trimers are suppressed.

The analogies to the Hubbard dimer are thereby particularly evident. We can identify the band insulator observed on the diagonal in Fig. 4(a-d) with the $A = 1$ bonding regime and the Mott insulator at low $V_{\mathrm{tr}}/U_{\mathrm{tr}}$ with the correlated high $A$ regime. Importantly, our results indicate a continuous crossover between the two different insulating states of the LT phase, which is reflected in all observables examined.

Finally, we further exemplify this evolution by showing the spectral function at a fixed value of $U_{\mathrm{tr}}$ and different values of $V_{\mathrm{tr}}$, projected on suitably constructed bonding and antibonding dimer orbitals [Fig. 4(e, f)]. We observe that the two peaks change their character with increasing $V_{\mathrm{tr}}$. The lower peak becomes predominantly bonding, while the upper peak becomes more antibonding as $V_{\mathrm{tr}}$ increases. Due to inherent difficulties in the analytic continuation and the large size of the gap, the spectral function shows smooth peaks across the spectrum, and we are not able to resolve finer spectral details such as the splitting of the Hubbard peaks that was observed, e.g., in the work of Aretz *et al.* [38].

These results provide evidence that the physics of the $R\bar{3}m$ phase of $Nb_3Cl_8$ and the $Nb_3X_8$ family in general can be described by dimers of $Nb_3$ molecular units, which are weakly coupled to each other. These findings support the results from the previous sections and indicate the presence of strong local antiferromagnetic correlations which could be ul-

ARTICLE IN PRESS

timately responsible for the suppression of the magnetic susceptibility in $\beta$-$Nb_3Cl_8$, as has been suggested previously [38]. The additional analysis of the $U$ and $V$ dependence sheds light on the evolution of this state under stronger electronic correlation effects. Moreover, we explicitly demonstrate a continuous crossover between the Mott and singlet (band) insulating states, in line with recent theoretical proposals [25, 45, 46]. The cRPA calculations indicate that $Nb_3Cl_8$ itself lies closer to the Mott limit, while the rest of the family lies closer to the singlet (band) insulating limit [see SI [20], Supplementary Table 3 and Supplementary Fig. 3 for the rest of the family].

## Further symmetry lowering in the $\beta$-$Nb_3Cl_8$ phase

We will now consider the case of a system very close to the Mott regime, with relatively little intertrimer hybridization as a starting point to understand further symmetry lowering effects, analyzing the physics within the $Nb_3$ unit. By incorporating all six bands between 1.2 eV and $-0.5$ eV [as shown in Fig. 5(b), corresponding to the $2a_1$ and $2e$ levels in Fig. 1(d)] in the wannierization, we construct a basis set consisting of one $d$ atomic orbital per Nb atom, yielding a total of three $d$ orbitals per $Nb_3$ trimer [as shown in Fig. 5(a)] and six $d$ orbitals per unit cell [47].

Using cRPA, we calculated the relevant, now atomic, interaction parameters (see SI [20], Supplementary Table 3): the onsite interaction on a single Nb atom, $U_{\mathrm{at}} = 2.3$ eV, the intratrimer interaction between two different Nb atoms inside the same trimer, $V_{\mathrm{at}}^{\mathrm{intra}} = 1.36$ eV, and the intertrimer interaction between neighboring trimers, $V_{\mathrm{at}}^{\mathrm{inter}} = 0.39$ eV.

Leveraging our previous finding that the intertrimer occupation is small in the Mott regime, leading to electron localization on the trimer, we neglect the interaction across trimers ($V_{\mathrm{at}}^{\mathrm{inter}}$) for simplicity. We then perform DFT+DMFT calculations considering two separate impurity problems, with each impurity containing the three Nb $d$ orbitals, including $U_{\mathrm{at}}$ and $V_{\mathrm{at}}^{\mathrm{intra}}$ in the interaction Hamiltonian [see Eq. (8) for further details].

While DFT calculations distribute the single electron per each trimer equally among the

ARTICLE IN PRESS

Nb atoms, leading to an oxidation state of $Nb^{8/3+}$, in our charge self-consistent DFT+DMFT calculations we observe that for realistic values of $(U_{at}, V_{at}^{intra})$ most of the charge concentrates on one of the Nb atoms [see Fig. 5(e) for 0.0 Å scissoring]. This charge ordering within the trimer changes the nominal oxidation states of the three Nb atoms and renders them inequivalent: for every $Nb_3$ trimer we obtain one nominal $Nb^{2+}$ site and two empty $Nb^{3+}$ sites.

Our results also indicate that the structure accommodates this change in oxidation state within each trimer by elongating the bond length $d'$ between the nominal $Nb^{3+}$ and $Nb^{2+}$ atoms and contracting the bond length $d''$ between the two $Nb^{3+}$ atoms [see Fig. 5(c)]. The difference, $d' - d''$, is termed *scissoring*. This scissoring distortion lowers the symmetry from $R\bar{3}m$ to $C2/m$, precisely matching both our own (see next section) and previous experimental work by Sheckelton *et al.* [31].

This can be seen from Fig. 5(d, e), where we show the energy per unit cell and the occupation of the nominal $Nb^{2+}$ and $Nb^{3+}$ calculated at every step of the scissoring mode. We consider various values of $U_{at}$, while maintaining a constant ratio of $V_{at}^{intra}/U_{at} = 0.24$ (corresponding to our cRPA results). However, it is worth noting that our results exhibit weak dependence on the value of $V_{at}^{intra}$, and similar outcomes can be obtained by setting $V_{at}^{intra} = 0$.

For $U_{at} = 0\,\text{eV}$, the scissoring changes the occupation of the Nb atoms only slightly [Fig. 5(e), gray line], and the system always relaxes back to $R\bar{3}m$ symmetry. For all finite values of $U_{at}$ considered, the system shows strong electron charge concentration on the nominal $Nb^{2+}$ atom [Fig. 5(e), colored lines], and an energy minimum at a finite scissoring distortion [Fig. 5(d)]. As $U_{at}$ increases, the energy minimum deepens and shifts towards a larger scissoring amplitude, while the occupation of the $Nb^{2+}$ atom becomes closer to 1. The scissoring distortion hence increases the onsite energy difference between the nominally $Nb^{2+}$ and $Nb^{3+}$ atomic sites (see SI [20], Supplementary Fig. 2).

Compared to the results of Sheckelton *et al.* [31], our calculated equilibrium scissoring

ARTICLE IN PRESS

amplitude is markedly smaller. For $U_{\mathrm{at}} = 2.3$ eV [orange solid line in Fig. 5(d)], we find ∼0.04 Å, versus 0.14 Å reported in Ref. [31] [indicated by the vertical black line in Fig. 5(d)].

As a remark, we also note that comparable results can be obtained through simpler DFT+$U$ calculations, utilizing standard orthonormalized atomic orbitals as implemented in QUANTUM ESPRESSO [48]. If one starts an atomic relaxation with a small scissoring distortion and initializes the entire magnetic moment on a single Nb atom per $Nb_3$ trimer (and ensuring that the two magnetic Nb atoms in a unit cell containing two trimers are initialized with opposite magnetization), then for realistic values of the Hubbard $U$ parameter, the system relaxes to $C2/m$ symmetry. This $C2/m$ phase is lower in energy than the antiferromagnetic $R\bar{3}m$ phase, where the magnetization is uniformly spread over the trimer, and it exhibits a scissoring mode amplitude similar to that found in our DFT+DMFT calculations, with most of the trimer's magnetization concentrated on the nominal $Nb^{2+}$ atom. We note that in the DFT+$U$ calculations, an artificial antiferromagnetic order has to be imposed, which is not observed in the real material.

In this section, we have demonstrated the possibility of additional ordering in $\beta$-$Nb_3Cl_8$ arising from the internal structure of the $Nb_3$ unit. Since the amplitude of the scissoring distortion is dependent on the value of $U_{\mathrm{at}}$, and given that intertrimer bonding components become more relevant for other members of the $Nb_3X_8$ family, the approximation of being deep in the Mott state may break down in those cases. We would then expect this scissoring tendency to be less pronounced across the rest of the series, which aligns with experimental observations, having previously found the $C2/m$ phase only in $Nb_3Cl_8$. Hence, we now turn to our experimental results for $Nb_3Cl_8$ and the mixed $Nb_3Cl_4Br_4$ compound.

## Experimental

In order to validate the results of our computational investigation of $Nb_3Cl_8$, and to attempt to understand the origins of the differing LT phases reported in the literature, we have synthesized $Nb_3Cl_8$ and $Nb_3Cl_4Br_4$ and characterized their crystallographic structure and

ARTICLE IN PRESS

electronic properties. Our samples of $Nb_3Cl_8$ were determined by single crystal XRD to adopt the HT $P\bar{3}m1$ phase at 100 K, the lowest temperature at which we could perform these measurements. Magnetic susceptibility measurements (see SI [20], Supplementary Fig. 7) on a single crystal show the phase transition to occur below 100 K on cooling and slightly above 100 K on heating, and our finding of the HT phase at 100 K is therefore ascribed to hysteresis of the phase transition.

Therefore, in order to observe the LT phase, we prepared $Nb_3Br_{4-x}Cl_{4+x}$, which was determined to have an increased phase transition temperature by Pasco *et al.* [30]. However, whereas the authors observed a LT $R\bar{3}m$ phase, we found the LT structure to adopt $C2/m$ (Table 1, Fig. 6), indicating that the space group of LT $Nb_3Cl_4Br_4$, like that of LT $Nb_3Cl_8$, possesses some ambiguity.

Notably, our synthetic method, which employed only elemental Nb, $NbCl_5$ and $NbBr_5$ as reagents, follows that of Sheckelton *et al.* [31], who found the $C2/m$ phase in $Nb_3Cl_8$ at low temperatures. In contrast, synthesis using a transport agent such as $NH_4Cl$ or $TeCl_4$ were reported to yield a LT $R\bar{3}m$ phase [30, 32], whereas reports of the $R3$ phase are associated with flux growth in $PbCl_3$ followed by soaking in hot water [28, 34]. These associations suggest that the precise LT phase adopted by $Nb_3Cl_8$ and $Nb_3Br_{4-x}Cl_{4+x}$ could be determined by the synthetic conditions. In particular, tellurium has been reported to incorporate itself into the $Nb_3Cl_8$ structure by capping $Nb_3$ triangles [49], and the introduction of defects has been suggested to trap $Nb_3Br_8$ in its HT phase [30]; a similar effect related to the introduction of impurities from the transport agent could push the material into the $R\bar{3}m$ phase, which is more closely related to the HT $P\bar{3}m1$ phase than the $C2/m$ is.

The changes between trimers in adjacent layers in $Nb_3Cl_4Br_4$ following the phase transition can be readily seen in the single-crystal XRD refinements. At 270 K, the intertrimer distances are at 755.98(5) pm and 746.06(5) pm (Fig. 6, left). In the low temperature structure (at 100 K), these distances alternate between 639.99(2) pm and 743.64(2) pm (Fig. 6, right), leading to the stacking shift (Fig. 1b) which modifies the intercluster interactions

ARTICLE IN PRESS

(Fig. 1c).

At 270 K, in the $P\bar{3}m1$ phase, the Nb–Nb distances within a cluster form equilateral triangles with bond lengths of 284.97(6) pm (Fig. 7, top). In the low-temperature $C2/m$ phase at 100 K, the clusters adopt an isosceles triangular arrangement, with one Nb–Nb bond measuring 284.61(8) pm and the other two at 284.45(8) pm (Fig. 7, bottom). The asymmetry arises due to the unambiguous loss of 3-fold rotational symmetry upon cooling, but the overall change in bond lengths remains very small, to the point where one short and two long Nb–Nb bonds is possible within the experimental uncertainty. The difference in Nb–Nb bond lengths is much smaller in $Nb_3Cl_4Br_4$ than was reported by Sheckelton *et al.* in $Nb_3Cl_8$ [31]. According to our computational results discussed in the previous section, the change in the stacking sequence observed in Fig. 6 is driven by intertrimer interaction, while the symmetry reduction to $C2/m$, which removes the 3-fold rotation axis and allows the Nb–Nb bond lengths to differ, is likely a secondary effect driven by intratrimer interactions.

We conducted magnetic measurements on $Nb_3Cl_8$ to observe the phase transition, as this occured below the minumum temperature at which we could perfom crystallographic measurements. We see a similar phase transition temperature (*ca.* 100 K) and degree of hysteresis (see SI [20], Supplementary Fig. 7) to previous reports of single crystals of $Nb_3Cl_8$ [28, 31, 32]. However, unlike Haraguchi *et al.* [28], who observed this transition only in single crystals, we were able to detect a magnetic phase transition in both single crystal and powder samples (see SI [20], Supplementary Fig. 8). In comparison to the single crystal sample, the powder sample displays an increased hysteresis, and a stronger temperature dependence of the paramagnetic response below the transition temperature. This temperature dependence leads to suppression of the paramagnetism near the transition temperature upon heating, a phenomenon also observed in assemblages of single crystals [30], suggesting that inter-grain interactions affect the magnetic properties of $Nb_3Cl_8$.

Optical measurements were performed above the structural transition temperature at room temperature. For both $Nb_3Cl_8$ and $Nb_3Cl_4Br_4$, we observe similar direct and indirect

ARTICLE IN PRESS

optical band gaps (see Table 2), based on measurements on bulk samples consisting of small crystallites. This result indicates similar electronic properties of $Nb_3Cl_8$ and $Nb_3Cl_4Br_4$, validating our use of $Nb_3Cl_4Br_4$ as a proxy for low-temperature structural measurements. The values are consistent with literature reports [12, 50] but are smaller compared to our DFT+DFMT results.

We investigated the temperature-dependent conductivity of bulk crystals and observed semiconducting behavior (see SI [20], Supplementary Fig. 6) for the high temperature modification above 100 K. The conductivity ranges from approximately $2 \times 10^{-3}$ S·m$^{-1}$ at 300 K to $8 \times 10^{-8}$ S·m$^{-1}$ at 100 K. Below 100 K, the conductivity fell below the detection limit. No hysteresis was observed during cooling and heating cycles, which is consistent with the measurements being conducted above the structural transition temperature. As the magnetic susceptibility shows some hysteresis above 100 K (see SI [20], Supplementary Fig. 7), our experimental results suggest that the electrical conductivity is not strongly affected by the magnetic transition, further indicating that the magnetic transition is not driven by charge disproportionation. Our results algin with the earlier measurements by Yoon *et al.* [12] at higher temperatures.

ARTICLE IN PRESS

## Discussion

In this work, we performed a DFT+$U$+$V$, DFT+DMFT, and experimental study of the bulk LT $\beta$-$Nb_3Cl_8$ phase. Particularly, we studied the different proposed mechanisms of the observed magnetostructural transition, with a focus on the effects of intra- and intertrimer Coulomb interactions.

We showed that it is the dimerization of the layers due to the change in stacking that is the primary driver of the magnetic transition in these compounds and that the charge disproportionation model [28, 34] is not consistent with our calculations. In particular, through a DFT+DMFT analysis we show that $Nb_3Cl_8$ behaves as a system of weakly-coupled Hub-

ARTICLE IN PRESS

bard dimers, and that two of the proposed explanations for the physics of $Nb_3Cl_8$, the Mott-like strongly antiferromagnetically coupled system, and the singlet-like band insulator are smoothly connected, with the intertrimer interaction dictating their crossover. Additionally, the analysis of the intratrimer behavior suggests a possible mechanism for the experimentally observed scissoring of the trimer units.

The important role of the intertrimer interaction manifests itself also in the other members of the $Nb_3X_8$ family [see SI [20], Supplementary Table 2] where a smaller $U/t$ ratio leads to a larger proximity to the band insulator solution rather than a Mott-like behavior.

In line with the theoretical findings, single-crystal X-ray diffraction reveals a structural phase transition in $Nb_3Br_4Cl_4$ from $P\bar{3}m1$ to $C2/m$, accompanied by a pronounced reduction in the distances between adjacent clusters. The bond lengths within the $Nb_3$ clusters slightly decrease upon cooling across the transition. Symmetry breaking leads to a slight distortion of the equilateral $Nb_3$ triangles into isosceles ones. However, the difference between the shorter and longer Nb–Nb bond lengths remains small and experimentally does not indicate a clear preference regarding whether the one inequivalent bond is longer or shorter than the others. The primary structural effect detected by our X-ray diffraction study is therefore a rearrangement of clusters of adjacent layers relative to one another, rather than significant changes within the clusters themselves. Magnetic measurements on $Nb_3Cl_8$ confirm the expected magnetic-to-nonmagnetic transition around 90 K, with clear hysteresis observed in both single crystals and powder samples. Temperature-dependent conductivity measurements showed a gradual decrease upon cooling to the transition temperature, without significant hysteresis. Below 100 K, no current could be detected within the sensitivity of the measurement setup. The differing hysteresis behavior of the magnetic and electric properties is consistent with our computational results, in particular the absence of interlayer charge disproportionation.

In conclusion, our work provides further evidence that the magnetostructural transition in LT $\beta$-$Nb_3Cl_8$ is driven primarily by a change in crystal stacking to the $R\bar{3}m$ phase. The

ARTICLE IN PRESS

physics of this interlayer dimerization can be understood in terms of weakly-coupled Hubbard dimers formed from pairs of Nb trimers. The subtle competition between intratrimer and intertrimer interactions tunes the system across a crossover between the limits of a Mott insulator and a band insulator. Concurrently, Coulomb interactions within a trimer drive a secondary, more subtle scissoring distortion within the $Nb_3$ trimer units.

This mechanism highlights the general importance of interlayer coupling in determining the electronic and magnetic properties of the $Nb_3X_8$ family of materials. Our calculations suggest that targeted control of external parameters such as pressure, chemical substitution, or strain, might allow systematic exploration of the crossover from Mott to band insulator and engineering of new functionalities in this and related cluster Mott systems.

# Methods

## DFT+$U$+$V$ calculations

We perform DFT+$U$+$V$ calculations using the QUANTUM ESPRESSO package (v6.6) [48, 51] within the generalized gradient approximation with the Perdew-Burke-Ernzerhof [52] exchange-correlation functional, utilizing the semiempirical DFT-D3 correction [53] to account for the van der Waals effects. We use the scalar-relativistic ultrasoft pseudopotentials from the GBRV library [54] with semicore 4$s$ and 4$p$ states included as valence for the Nb atoms.

We construct a localized set of orbitals using WANNIER90 (v3.1.0) [55, 56]. Starting from a conventional non-spin-polarized DFT calculations, we consider the two bands in close proximity to the Fermi level with dominant Nb contributions and with no entanglement with the surrounding bands [see Fig. 1(e)]. Following Grytsiuk *et al.* [21], our basis set consists of two trimer-centered Wannier functions computed by projecting the Kohn-Sham (KS) states around the Fermi level onto initial guesses of $d_{z^2}$ orbitals and performing subsequent orthonormalization to finally obtain the molecular trimer orbitals shown in Fig. 1(f). All

ARTICLE IN PRESS

structural and Wannier function visualizations were produced using VESTA [57].

We then employ these trimer orbitals in both spin-unpolarized and spin-polarized DFT+$U$+$V$ calculations using the implementation from Ref. [42]. We consider both onsite (intratrimer) and intersite (intertrimer) interactions described by parameters $U_{\rm tr}$ and $V_{\rm tr}$, respectively [see Fig. 1(c)].

When performing structural variation, the Wannier functions are recalculated at every step.

## DFT+DMFT calculations

The trimer basis set for the DFT+DFMT calculations is described by the same Wannier functions obtained in the previous section. We consider an impurity problem composed of two adjacent trimer orbitals, a "dimer of trimers", for which the Hamiltonian reads:

$$H = H_0 + H_{\rm int} - H_{\rm DC}, \tag{5}$$

where $H_0$ corresponds to the effective single-particle DFT Hamiltonian as obtained in the wannierization procedure and $H_{\rm int}$ is the interaction Hamiltonian:

$$H_{\rm int} = U_{\rm tr} \sum_i \hat{n}_i^{\uparrow} \hat{n}_i^{\downarrow} + V_{\rm tr} \sum_{\langle ij \rangle, \sigma\sigma'} \hat{n}_i^{\sigma} \hat{n}_j^{\sigma'}, \tag{6}$$

where $\hat{n}_i^{\sigma}$ is the spin resolved number operator for trimer site $i$ and spin $\sigma$. The meaning of $U_{tr}$ and $V_{tr}$ corresponds to the same as in the DFT+$U$+$V$ case, that of an onsite (intratrimer) and intersite (intertrimer) interaction, respectively.

$H_{\rm DC}$ is the double-counting (DC) term, which cancels out the part of local interaction already included in the $H_0$ term [40]. Here, we employ the standard fully-localized limit for the expression of the energy of the double counting correction [58], which in this basis set,

ARTICLE IN PRESS

translates to a constant shift of the trimer orbital energies:

$$\Sigma^{tr}_{\mathrm{DC}} = U \sum_{i,\sigma} \left( N_i^{\mathrm{tr}} - \frac{1}{2} \right) \hat{n}_i^{\sigma}. \tag{7}$$

Here, $N_i^{\mathrm{tr}} = \sum_\sigma \langle n_i^\sigma \rangle$ is the occupation of the trimer orbitals. In the presence of a difference in occupation between the two trimers, i.e., a charge disproportionation scenario, this term could in principle favor the localization of two electrons on one trimer. However, similarly to the DFT+$U$+$V$ calculations, we find no trace of this tendency in our DFT+DMFT calculations and both trimers remain equally occupied. We note that we have not included an intersite contribution to the double-counting potential. The approach outlined in Ref. [40] and used in the DFT+$U$+$V$ calculations, effectively removes the double counting of the Hartree contribution stemming from intersite interactions, which would further suppress charge-disproportionation in the present case. However, given that our DFT+DMFT calculations already show no tendency for charge order and maintain equally occupied trimers, we do not anticipate that including this term would have any effect on our results.

In the atomic basis, we construct Wannier functions including all 6 bands in the energy range between $-0.5$ eV and 1.5 eV around the Fermi level. This results in one $d$ orbital per Nb site oriented towards the center of the trimer. We then perform DFT+DMFT calculations with 2 impurity models, each one including the 3 atomic orbitals belonging to one $Nb_3$ unit. The resulting Hamiltonian has the same form as described in Eq. (5), however, the $H_0$ term this time represents the tight binding model described by the atomic Wannier basis set, and $H_{\mathrm{int}}$ reads:

$$H_{\mathrm{int}} = U_{\mathrm{at}} \sum_i \hat{m}_i^{\uparrow} \hat{m}_i^{\downarrow} + V_{\mathrm{at}}^{\mathrm{intra}} \sum_{\langle ij \rangle, \sigma\sigma'} \hat{m}_i^{\sigma} \hat{m}_j^{\sigma'}, \tag{8}$$

where now $\hat{m}_i^\sigma$ is the number operator for an atomic orbital on Nb site $i$ and spin channel sigma $\sigma$, and $V_{\mathrm{at}}^{\mathrm{intra}}$ is the Nb-Nb interaction inside one trimer. For the DC correction we

ARTICLE IN PRESS

again employ the fully-localized limit, but this time in the atomic basis:

$$\Sigma^{at}_{\mathrm{DC}} = \sum_i U\left(M_i^{\mathrm{at}} - \frac{1}{2}\right)\hat{m}_i^{\sigma} \quad , \tag{9}$$

where $M_i^{\mathrm{at}} = \sum_\sigma \langle m_i^\sigma \rangle$. This terms translates to a downward energetic shift of the occupied atoms and an upward shift of the unoccupied ones.

In our DMFT calculations for the three-atom clusters, we have again omitted the intersite contribution to the double-counting corrections. Given that the material is deep in the Mott regime, the strong Coulomb interaction enforces a local filling of exactly one electron per $Nb_3$ cluster. The subspace of relevant electronic configurations is therefore composed almost exclusively of states with a single occupied atomic orbital per trimer. Within this subspace, the Hamiltonian term for the intersite interaction, $V_{at}^{\mathrm{intra}} \sum_{ij} m_i^\sigma m_j^{\sigma'}$, always acts as the zero operator and, in fact, we performed benchmark calculations and we see negligble effect of the value of $V_{\mathrm{at}}^{\mathrm{intra}}$. In this sense, since the $V_{\mathrm{at}}^{\mathrm{intra}}$ does not seem to contribute to the self-energy, we deem the introduction of an inter-atomic DC correction unnecessary.

All our DFT+DMFT calculations are fully charge self-consistent and were performed using `solid_dmft` [59], which is part of the TRIQS library [60]. We solve all the DMFT impurity problems with the continuous-time quantum Monte Carlo solver CT-HYB [61–63] at the inverse electronic temperature close to room temperature of $\beta = (k_B T)^{-1} = 40\mathrm{eV}^{-1}$. We note that this is purely the electronic temperature of the chosen solver. We use $10^4$ warm-up steps and $2 \times 10^8$ Monte Carlo cycles with 120 steps each. We average over both spin channels to ensure a paramagnetic solution.

From the local Green's function, $G_{\nu\nu'}(\tau)$, where $\nu$, $\nu'$ correspond to different orbitals and $\tau$ is the imaginary time, we obtain the local occupations on a given site (trimer), $n_{\nu\nu'} = G_{\nu\nu'}(\tau = 0^-)$, as well as the averaged spectral weight around the Fermi level, $\bar{A}(\omega = 0) = -(\beta/\pi)\mathrm{Tr}G(\tau = \beta/2)$. Additionally, we calculate the quasiparticle weight, $Z = [1 - \partial \mathrm{Im}\Sigma(i\omega)/\partial(i\omega)|_{i\omega\to 0}]^{-1}$, from the imaginary part of the local self-energy, $\Sigma$, by

ARTICLE IN PRESS

fitting a third-order polynomial to the lowest five Matsubara frequencies and interpolating to zero frequency. Finally, we use the maximum-entropy method [64, 65] to obtain the $k$-averaged spectral functions on the real frequency axis.

## cRPA calculations

For the cRPA calculations, norm-conserving pseudopotentials from PSEUDODOJO [66, 67] are used to perform the initial DFT calculations. For these, we use a kinetic energy cutoff of 52 Ry (∼700 eV) and 12×52 Ry for the charge density. We converge the total energies to $10^{-3}$ Ry using a 6×6×3 $k$-point, smearing the occupations with the Marzari-Vanderbilt scheme [68] with smearing parameter of 0.001 Ry.

Screened Coulomb interaction parameters are obtained using the cRPA code RESPACK [69], using the WAN2RESPACK interface to QUANTUM ESPRESSO [70]. We set the polarization function cutoff to 15 Ry and we use a total of 300 bands, setting the upper limit of the highest possible excitations to 25 eV above the Fermi energy.

## Experimental details

For the synthesis of $Nb_3Cl_8$, a mixture of $NbCl_5$ (76.9 mg, 28.4 mmol ABCR GmbH, 99.9%) and Nb (23.1 mg, 24.9 mmol, ABCR GmbH, 99.9%), fused into an evacuated silica tube, was heated with 0.5 K/min in a Simon-Müller furnace. After heating at 750 °C for 48 hours, $Nb_3Cl_8$ was obtained as plate-like crystals (yield: $> 95$ %).

For the synthesis of $Nb_3Br_4Cl_4$, a mixture of $NbBr_5$ (79.8 mg, 16.2 mmol, ABCR GmbH, 99.9%), $NbCl_5$ (43.8 mg, 16.2 mmol ABCR GmbH, 99.9%) and Nb (26.4 mg, 28.4 mmol, ABCR GmbH, 99.9%), fused into an evacuated silica tube, was heated with 0.5 K/min in a Simon-Müller furnace. After heating at 750 °C for 48 hours, $Nb_3Br_4Cl_4$ was obtained as plate-like crystals (yield: $> 90$ %).

Single-crystal x-ray diffraction was used for structure characterization. To maintain crystal integrity, separate single crystals were selected for each measurement and gradually cooled

ARTICLE IN PRESS

to the target temperature at a rate of 2 K/min. Data collection was performed on a Rigaku XtaLAB Synergy-S single-crystal X-ray diffractometer equipped with HyPix-6000HE detector and monochromated Mo-$K_\alpha$ radiation ($\lambda = 71.037$ pm ) at 100 K and monocromated Cu-$K_\alpha$ radiation ($\lambda = 154.184$ pm) at 270 K. X-ray intensities were corrected for absorption with a numerical method (crystal faces) using CrysAlisPro 1.171.43.121a (Rigaku Oxford Diffraction, 2024). Structures were solved by direct methods (SHELXT) and refined by full-matrix least squares methods performed with SHELXL-2019/3 [71] as implemented in Olex2 1.5 [72]. Detailed crystallographic data can be obtained free of charge via www.ccdc.cam.ac.uk and the CCDC numbers.

Electrical conductivity measurements were performed in a Lake Shore Cryotronics CRX-6.5K probe station with a Keithley 2636B source meter unit. Plate-like crystals of $Nb_3Cl_8$ were transferred into the chamber under protective gas and contacted with silver paste on a silicon substrate with 770 nm oxide layer. The conductive silver pads at each end of the crystals were connected to the circuit with gold coated tungsten tips. The chamber was kept under vacuum ($> 5 \cdot 10^{-5}$ mbar) and the temperature was varied between 20 K and 300 K (see SI [20], Supplementary Fig. 6). Before each measurement, sufficient time was allowed for the sample to reach the chosen temperature. Two-point conductivity measurements were performed by varying the applied source–drain voltage from -1 V to 1 V while detecting the current.

DRIFT (Diffuse Reflectance Infrared Fourier Transformation Spectroscopy) samples were measured at room temperature under inert conditions in diffuse reflectance with a Harrick Praying Mantis attachment using a Bruker Vertex 70 infrared spectrophotometer with a deuterated triglycine sulfate (DTGS) detector and KBr beamsplitter. The background spectra were collected using pure dried KI in powder form.

Magnetic susceptibility measurements of crystalline powders and single crystals were performed in gelatine capsules between 5 K and 300 K with a Quantum design SQUID magnetometer equipped with a 1802 R/G bridge and a 1822 MDMS controller.

ARTICLE IN PRESS

## Data availability

The data from the DFT+$U$+$V$ and DFT+DMFT calculations presented in this study is available at https://zenodo.org/records/17898535.

## Acknowledgments

The authors thank S. Grytsiuk, J. Aretz, M. Rösner, and M. I. Katsnelson for valuable discussions and initial input files. Calculations were performed on the "Euler" cluster of ETH Zürich and the Swiss National Supercomputing Center Eiger cluster under Project ID s1304. We would like to thank Dr. F. Strauß for conducting and analyzing the conductivity measurements and Prof. M. Scheele for providing access to the necessary equipment. We also thank Dr. J. Glaser for conducting and analyzing the magnetic measurements.

P.M. and N.A.S. acknowledge funding from the Swiss National Science Foundation (Grant number 209454) and from ETH Zürich. C.P.R. acknowledges support from the project FerrMion of the Ministry of Education, Youth and Sports, Czech Republic, co-funded by the European Union (CZ.02.01.01/00/22_008/0004591).

ARTICLE IN PRESS

## Author contributions

A.C., P.M., and C.P.R. conceptualized the project. A.C. and P.M. performed the calculations. F.G., M.S., and H.-J.M. conceptualized and performed the experiments. A.C., P.M., C.P.R., and F.G. wrote the first manuscript version. A.C., P.M., F.G., M.S., H.-J.M., C.P.R., N.A.S., and C.E. contributed to the discussion and interpretation of the results and to the writing of the manuscript. All authors have read and approved the manuscript.

ARTICLE IN PRESS

## Competing interests

The authors declare no competing financial or non-financial interests.

ARTICLE IN PRESS

ARTICLE IN PRESS

# References


(1) Roy, S. B. *Mott Insulators: Physics and applications*; IOP Publishing, 2019.

(2) Müller, H.; Kockelmann, W.; Johrendt, D. The magnetic structure and electronic ground states of Mott insulators $GeV_4S_8$ and $GaV_4S_8$. *Chem. Mater.* **2006**, *18*, 2174–2180.

(3) Kimber, S. A. J.; Senn, M. S.; Fratini, S.; Wu, H.; Hill, A. H.; Manuel, P.; Attfield, J. P.; Argyriou, D. N.; Henry, Paul. F. Charge order at the frontier between the molecular and solid states in $Ba_3NaRu_2O_9$. *Phys. Rev. Lett.* **2012**, *108*, 217205.

(4) Nag, A.; Middey, S.; Bhowal, S.; Panda, S. K.; Mathieu, R.; Orain, J. C.; Bert, F.; Mendels, P.; Freeman, P. G.; Mansson, M. et al. Origin of the spin-orbital liquid state in a nearly $J$=0 iridate $Ba_3ZnIr_2O_9$. *Phys. Rev. Lett.* **2016**, *116*, 097205.

(5) Streltsov, S. V.; Cao, G.; Khomskii, D. I. Suppression of magnetism in $Ba_5AlIr_2O_{11}$: Interplay of Hund's coupling, molecular orbitals, and spin-orbit interaction. *Phys. Rev. B* **2017**, *96*, 014434.

(6) Jayakumar, V.; Hickey, C. Elementary building blocks for cluster Mott insulators. *Phys. Rev. B* **2026**, *113*, 035151.

(7) Grahlow, F.; Strauß, F.; Schmidt, P.; Valenta, J.; Ströbele, M.; Scheele, M.; Romao, C. P.; Meyer, H.-J. $Ta_4SBr_{11}$: A cluster Mott Insulator with a corrugated, van der Waals layered structure. *Inorg. Chem.* **2024**, *63*, 19717–19727.

(8) Nikolaev, S. A.; Solovyev, I. V.; Streltsov, S. V. Quantum spin liquid and cluster Mott insulator phases in the $Mo_3O_8$ magnets. *npj Quantum Mater.* **2021**, *6*, 1–8.

(9) Hu, J.; Zhang, X.; Hu, C.; Sun, J.; Wang, X.; Lin, H.-Q.; Li, G. Correlated flat bands and quantum spin liquid state in a cluster Mott insulator. *Commun. Phys.* **2023**, *6*, 1–8.


ARTICLE IN PRESS

ARTICLE IN PRESS

(10) Liu, B.; Zhang, Y.; Han, X.; Sun, J.; Zhou, H.; Li, C.; Cheng, J.; Yan, S.; Lei, H.; Shi, Y. et al. Possible quantum-spin-liquid state in van der Waals cluster magnet $Nb_3Cl_8$. *J. Phys.: Condens. Matter* **2024**, *36*, 155602.

(11) Xu, Y.; Elcoro, L.; Song, Z.-D.; Vergniory, M. G.; Felser, C.; Parkin, S. S. P.; Regnault, N.; Mañes, J. L.; Bernevig, B. A. Filling-enforced obstructed atomic insulators. *Phys. Rev. B* **2024**, *109*, 165139.

(12) Yoon, J.; Lesne, E.; Sklarek, K.; Sheckelton, J.; Pasco, C.; Parkin, S. S. P.; McQueen, T. M.; Ali, M. N. Anomalous thickness-dependent electrical conductivity in van der Waals layered transition metal halide, $Nb_3Cl_8$. *J. Phys.: Condens. Matter* **2020**, *32*, 304004.

(13) Peng, R.; Ma, Y.; Xu, X.; He, Z.; Huang, B.; Dai, Y. Intrinsic anomalous valley Hall effect in single-layer $Nb_3I_8$. *Phys. Rev. B* **2020**, *102*, 035412.

(14) Feng, Y.; Yang, Q. Enabling triferroics coupling in breathing kagome lattice $Nb_3X_8$ (X = Cl, Br, I) monolayers. *J. Mater. Chem. C* **2023**, *11*, 5762–5769.

(15) Wu, H.; Wang, Y.; Xu, Y.; Sivakumar, P. K.; Pasco, C.; Filippozzi, U.; Parkin, S. S. P.; Zeng, Y.-J.; McQueen, T.; Ali, M. N. The field-free Josephson diode in a van der Waals heterostructure. *Nature* **2022**, *604*, 653–656.

(16) Oh, S.; Choi, K. H.; Chae, S.; Kim, B. J.; Jeong, B. J.; Lee, S. H.; Jeon, J.; Kim, Y.; Nanda, S. S.; Shi, L. et al. Large-area synthesis of van der Waals two-dimensional material $Nb_3I_8$ and its infrared detection applications. *J. Alloy Compd.* **2020**, *831*, 154877.

(17) Schäfer, H.; Schnering, H. G. Metall-Metall-Bindungen bei niederen Halogeniden, Oxyden und Oxydhalogeniden schwerer Übergangsmetalle Thermochemische und strukturelle Prinzipien. *Angew. Chem.* **1964**, *76*, 833–849.

ARTICLE IN PRESS

ARTICLE IN PRESS

(18) Magonov, S. N.; Zoennchen, P.; Rotter, H.; Cantow, H. J.; Thiele, G.; Ren, J.; Whangbo, M. H. Scanning tunneling and atomic force microscopy study of layered transition metal halides $Nb_3X_8$ (X = Cl, Br, I). *J. Am. Chem. Soc.* **1993**, *115*, 2495–2503.

(19) Ströbele, M.; Glaser, J.; Lachgar, A.; Meyer, H.-J. Struktur und elektrochemische Untersuchung von $Nb_3Cl_8$. *ZAAC* **2001**, *627*, 2002–2004.

(20) See the supplementary information provided with this article.

(21) Grytsiuk, S.; Katsnelson, M. I.; van Loon, E. G. C. P.; Rösner, M. $Nb_3Cl_8$: a prototypical layered Mott-Hubbard insulator. *npj Quantum Mater.* **2024**, *9*, 1–13.

(22) Gao, S.; Zhang, S.; Wang, C.; Yan, S.; Han, X.; Ji, X.; Tao, W.; Liu, J.; Wang, T.; Yuan, S. et al. Discovery of a single-band Mott Insulator in a van der Waals flat-band compound. *Phys. Rev. X* **2023**, *13*, 041049.

(23) Shan, P. F.; Han, X.; Li, X.; Liu, Z. Y.; Yang, P. T.; Wang, B. S.; Wang, J. F.; Liu, H. Y.; Shi, Y. G.; Sun, J. P. et al. Pressure-induced metallic state in a van der Waals cluster Mott insulator $Nb_3Cl_8$. *Mater. Today Phys.* **2023**, *38*, 101267.

(24) Nakamura, R.; Takegami, D.; Fujinuma, K.; Nakamura, M.; Ferreira-Carvalho, M.; Melendez-Sans, A.; Yoshimura, M.; Tsuei, K.-D.; Haraguchi, Y.; Aruga Katori, H. et al. Charge fluctuations in a cluster Mott state: Hard x-ray photoemission study on a breathing kagome magnet $Nb_3Cl_8$. *Phys. Rev. B* **2024**, *110*, L081109.

(25) Zhang, Y.; Gu, Y.; Weng, H.; Jiang, K.; Hu, J. Mottness in two-dimensional van der Waals $Nb_3X_8$ monolayers (X=Cl, Br, and I). *Phys. Rev. B* **2023**, *107*, 035126.

(26) Stepanov, E. A. Fingerprints of a charge ice state in the doped Mott insulator $Nb_3Cl_8$. *Phys. Rev. B* **2025**, *112*.

ARTICLE IN PRESS

ARTICLE IN PRESS

(27) Kennedy, J. R.; Adler, P.; Dronskowski, R.; Simon, A. Experimental and theoretical electronic structure investigations on $\alpha$-$Nb_3Cl_8$ and the intercalated phase $\beta$'-$NaNb_3Cl_8$. *Inorg. Chem.* **1996**, *35*, 2276–2282.

(28) Haraguchi, Y.; Michioka, C.; Ishikawa, M.; Nakano, Y.; Yamochi, H.; Ueda, H.; Yoshimura, K. Magnetic–nonmagnetic phase transition with interlayer charge disproportionation of $Nb_3$ trimers in the cluster compound $Nb_3Cl_8$. *Inorg. Chem.* **2017**, *56*, 3483–3488.

(29) Jiang, Z.; Jiang, D.; Wang, Y.; Li, C.; Liu, K.; Wen, T.; Liu, F.; Zhou, Z.; Wang, Y. Pressure-driven symmetry breaking and electron disproportionation of the trigonal $Nb_3$ cluster in $Nb_3Cl_8$. *Sci. China Phys. Mech. Astron.* **2022**, *65*, 278211.

(30) Pasco, C. M.; El Baggari, I.; Bianco, E.; Kourkoutis, L. F.; McQueen, T. M. Tunable magnetic transition to a singlet ground state in a 2D van der Waals layered trimerized Kagomé magnet. *ACS Nano* **2019**, *13*, 9457–9463.

(31) Sheckelton, J. P.; Plumb, K. W.; Trump, B. A.; Broholm, C. L.; McQueen, T. M. Rearrangement of van der Waals stacking and formation of a singlet state at T = 90 K in a cluster magnet. *Inorg. Chem. Front.* **2017**, *4*, 481–490.

(32) Kim, J.; Lee, Y.; Choi, Y. W.; Jung, T. S.; Son, S.; Kim, J.; Choi, H. J.; Park, J.-G.; Kim, J. H. Terahertz spectroscopy and DFT analysis of phonon dynamics of the layered Van der Waals semiconductor $Nb_3X_8$ (X = Cl, I). *ACS Omega* **2023**, *8*, 14190–14196.

(33) Regmi, S.; Sakhya, A. P.; Fernando, T.; Zhao, Y.; Jeff, D.; Sprague, M.; Gonzalez, F.; Bin Elius, I.; Mondal, M. I.; Valadez, N. et al. Observation of flat and weakly dispersing bands in the van der Waals semiconductor $Nb_3Br_8$ with breathing kagome lattice. *Phys. Rev. B* **2023**, *108*, L121404.

(34) Haraguchi, Y.; Yoshimura, K. Molecular orbital electronic instability in the van der

ARTICLE IN PRESS

Waals Kagomé semiconductor $Nb_3Cl_8$: exploring future directions. *J. Phys. Soc. Jpn.* **2024**, *93*, 111002.

(35) Morin, F. J. Oxides which show a metal-to-insulator transition at the Néel temperature. *Phys. Rev. Lett.* **1959**, *3*, 34–36.

(36) Goodenough, J. B. The two components of the crystallographic transition in $VO_2$. *J. Solid State Chem.* **1971**, *3*, 490–500.

(37) Eyert, V. The metal-insulator transitions of $VO_2$: A band theoretical approach. *Ann. Phys.* **2002**, *11*, 650–704.

(38) Aretz, J.; Grytsiuk, S.; Liu, X.; Feraco, G.; Knekna, C.; Waseem, M.; Dan, Z.; Bianchi, M.; Hofmann, P.; Ali, M. N. et al. From Strong to Weak Correlations in Breathing-Mode Kagome van der Waals Materials: $Nb_3(F,Cl,Br,I)_8$ as a Robust and Versatile Platform for Many-Body Engineering. *Phys. Rev. X* **2025**, *15*, 041042.

(39) Xiong, J.-X.; Zhang, X.; Zunger, A. Role of magnetic and structural symmetry breaking in forming the Mott insulating gap in $Nb_3Cl_8$. *Phys. Rev. B* **2025**, *111*, 155122.

(40) Leiria Campo Jr, V.; Cococcioni, M. Extended DFT+$U$+$V$ method with on-site and inter-site electronic interactions. *J. Phys.: Condens. Matter* **2010**, *22*, 055602.

(41) Kotliar, G.; Savrasov, S. Y.; Haule, K.; Oudovenko, V. S.; Parcollet, O.; Marianetti, C. A. Electronic structure calculations with dynamical mean-field theory. *Rev. Mod. Phys.* **2006**, *78*, 865–951.

(42) Carta, A.; Timrov, I.; Mlkvik, P.; Hampel, A.; Ederer, C. Explicit demonstration of the equivalence between DFT+$U$ and the Hartree-Fock limit of DFT+DMFT. *Phys. Rev. Res.* **2025**, *7*, 013289.

(43) Biermann, S.; Poteryaev, A.; Lichtenstein, A. I.; Georges, A. Dynamical singlets and correlation-assisted Peierls transition in $VO_2$. *Phys. Rev. Lett.* **2005**, *94*, 026404.

ARTICLE IN PRESS

(44) Pavarini, E., Koch, E., Scalettar, R., Martin, R., Institute for Advanced Simulation, German Research School for Simulation Sciences, Eds. *The physics of correlated insulators, metals, and superconductors*; Schriften des Forschungszentrums Jülich. Reihe Modeling and Simulation Band 7; Forschungszentrum, Zentralbibliothek: Jülich, 2017.

(45) Nájera, O.; Civelli, M.; Dobrosavljević, V.; Rozenberg, M. J. Multiple crossovers and coherent states in a Mott-Peierls insulator. *Phys. Rev. B* **2018**, *97*, 045108.

(46) Jiang, K.; Qi, Z.; Weng, H.; Hu, J. Mottness in obstructed atomic insulators without Mott transition. *Phys. Rev. B* **2023**, *108*, 195102.

(47) Streltsov, S. V.; Takegami, D.; Nakamura, R.; Kovaleva, P. P.; Poteryaev, A. I.; Nikolaev, S. A.; Xu, H.-H.; Sui, Y.; Yoshimura, M.; Tsuei, K.-D. et al. Beyond a cluster-Mott state in the breathing kagome lattice of $LiZn_2Mo_3O_8$. *Phys. Rev. B* **2025**, *111*, 085124.

(48) Giannozzi, P.; Andreussi, O.; Brumme, T.; Bunau, O.; Buongiorno Nardelli, M.; Calandra, M.; Car, R.; Cavazzoni, C.; Ceresoli, D.; Cococcioni, M. et al. Advanced capabilities for materials modelling with Quantum ESPRESSO. *J. Phys.: Condens. Matter* **2017**, *29*, 465901.

(49) Miller, G. J. Solid state chemistry of $Nb_3Cl_8$: $Nb_3TeCl_7$, mixed crystal formation, and intercalation. *J. Alloys Compd.* **1995**, *217*, 5–12.

(50) Date, M.; Petocchi, F.; Yen, Y.; Krieger, J. A.; Pal, B.; Hasse, V.; McFarlane, E. C.; Körner, C.; Yoon, J.; Watson, M. D. et al. Momentum-resolved fingerprint of Mottness in layer-dimerized $Nb_3Br_8$. *Nat. Commun.* **2025**, *16*, 4037.

(51) Giannozzi, P.; Baroni, S.; Bonini, N.; Calandra, M.; Car, R.; Cavazzoni, C.; Ceresoli, D.; Chiarotti, G. L.; Cococcioni, M.; Dabo, I. et al. QUANTUM ESPRESSO: A modular and open-source software project for quantum simulations of materials. *J. Phys.: Condens. Matter* **2009**, *21*, 395502.

ARTICLE IN PRESS

ARTICLE IN PRESS

(52) Perdew, J. P.; Burke, K.; Ernzerhof, M. Generalized gradient approximation made simple. *Phys. Rev. Lett.* **1996**, *77*, 3865–3868.

(53) Grimme, S.; Antony, J.; Ehrlich, S.; Krieg, H. A consistent and accurate ab initio parametrization of density functional dispersion correction (DFT-D) for the 94 elements H-Pu. *J. Chem. Phys.* **2010**, *132*, 154104.

(54) Garrity, K. F.; Bennett, J. W.; Rabe, K. M.; Vanderbilt, D. Pseudopotentials for high-throughput DFT calculations. *Comput. Mater. Sci.* **2014**, *81*, 446–452.

(55) Mostofi, A. A.; Yates, J. R.; Lee, Y.-S.; Souza, I.; Vanderbilt, D.; Marzari, N. wannier90: A tool for obtaining maximally-localised Wannier functions. *Comput. Phys. Commun.* **2008**, *178*, 685–699.

(56) Pizzi, G.; Vitale, V.; Arita, R.; Blügel, S.; Freimuth, F.; Géranton, G.; Gibertini, M.; Gresch, D.; Johnson, C.; Koretsune, T. et al. Wannier90 as a community code: new features and applications. *J. Phys.: Condens. Matter* **2020**, *32*, 165902.

(57) Momma, K.; Izumi, F. VESTA 3 for three-dimensional visualization of crystal, volumetric and morphology data. *J Appl Cryst* **2011**, *44*, 1272–1276.

(58) Anisimov, V. I.; Solovyev, I. V.; Korotin, M. A.; Czyżyk, M. T.; Sawatzky, G. A. Density-functional theory and NiO photoemission spectra. *Phys. Rev. B* **1993**, *48*, 16929–16934.

(59) Merkel, M. E.; Carta, A.; Beck, S.; Hampel, A. solid_dmft: gray-boxing DFT+DMFT materials simulations with TRIQS. *JOSS* **2022**, *7*, 4623.

(60) Parcollet, O.; Ferrero, M.; Ayral, T.; Hafermann, H.; Krivenko, I.; Messio, L.; Seth, P. TRIQS: A toolbox for research on interacting quantum systems. *Comput. Phys. Commun.* **2015**, *196*, 398–415.

ARTICLE IN PRESS

ARTICLE IN PRESS

(61) Werner, P.; Millis, A. J. Hybridization expansion impurity solver: General formulation and application to Kondo lattice and two-orbital models. *Phys. Rev. B* **2006**, *74*, 155107.

(62) Gull, E.; Millis, A. J.; Lichtenstein, A. I.; Rubtsov, A. N.; Troyer, M.; Werner, P. Continuous-time Monte Carlo methods for quantum impurity models. *Rev. Mod. Phys.* **2011**, *83*, 349–404.

(63) Seth, P.; Krivenko, I.; Ferrero, M.; Parcollet, O. TRIQS/CTHYB: A continuous-time quantum Monte Carlo hybridisation expansion solver for quantum impurity problems. *Comput. Phys. Commun.* **2016**, *200*, 274–284.

(64) Jarrell, M.; Gubernatis, J. E. Bayesian inference and the analytic continuation of imaginary-time quantum Monte Carlo data. *Phys. Rep.* **1996**, *269*, 133–195.

(65) Kraberger, G. J.; Triebl, R.; Zingl, M.; Aichhorn, M. Maximum entropy formalism for the analytic continuation of matrix-valued Green's functions. *Phys. Rev. B* **2017**, *96*, 155128.

(66) Hamann, D. R. Optimized norm-conserving Vanderbilt pseudopotentials. *Phys. Rev. B* **2013**, *88*, 085117.

(67) van Setten, M. J.; Giantomassi, M.; Bousquet, E.; Verstraete, M. J.; Hamann, D. R.; Gonze, X.; Rignanese, G. M. The PseudoDojo: Training and grading a 85 element optimized norm-conserving pseudopotential table. *Comput. Phys. Commun.* **2018**, *226*, 39–54.

(68) Marzari, N.; Vanderbilt, D.; De Vita, A.; Payne, M. C. Thermal Contraction and Disordering of the Al(110) Surface. *Phys. Rev. Lett.* **1999**, *82*, 3296–3299.

(69) Nakamura, K.; Yoshimoto, Y.; Nomura, Y.; Tadano, T.; Kawamura, M.; Kosugi, T.;

ARTICLE IN PRESS

Yoshimi, K.; Misawa, T.; Motoyama, Y. RESPACK: An ab initio tool for derivation of effective low-energy model of material. *Comput. Phys. Commun.* **2021**, *261*, 107781.

(70) Kurita, K.; Misawa, T.; Yoshimi, K.; Ido, K.; Koretsune, T. Interface tool from Wannier90 to RESPACK: wan2respack. *Comput. Phys. Commun.* **2023**, *292*, 108854.

(71) Sheldrick, G. M. Crystal structure refinement with SHELXL. *Acta Cryst. C* **2015**, *71*, 3–8.

(72) Dolomanov, O. V.; Bourhis, L. J.; Gildea, R. J.; Howard, J. a. K.; Puschmann, H. OLEX2: a complete structure solution, refinement and analysis program. *J. Appl. Cryst.* **2009**, *42*, 339–341.

ARTICLE IN PRESS

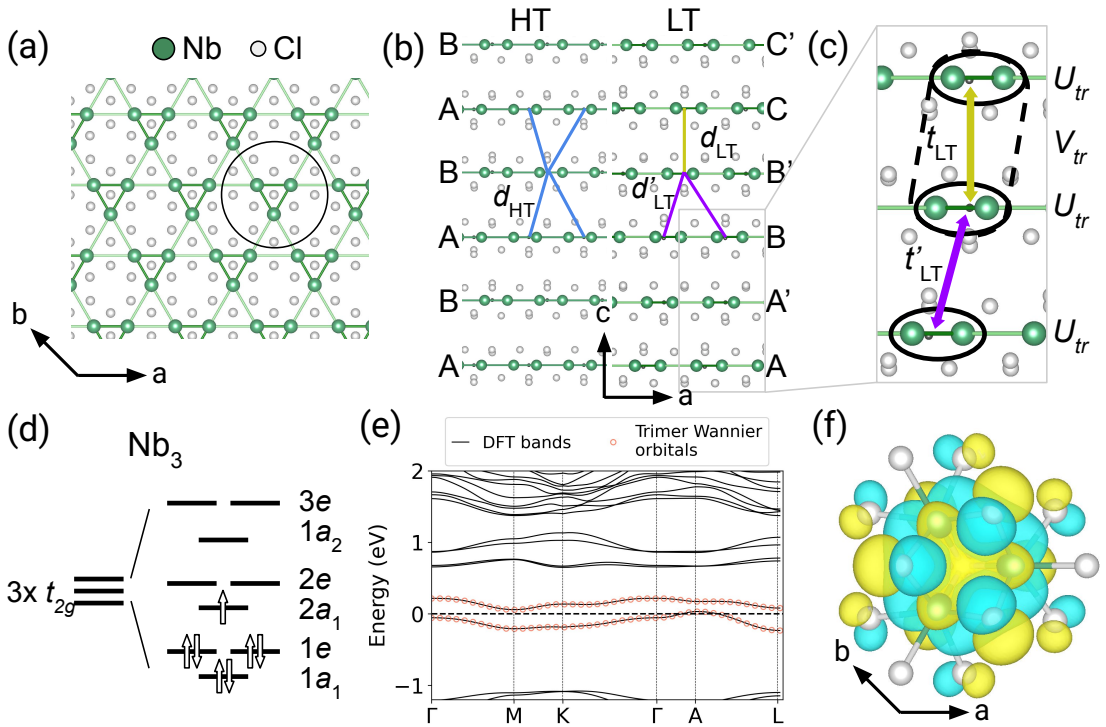



Figure 1: (a) Top view of the monolayer $Nb_3Cl_8$ with a trimer unit circled. (b) Side view of the bulk $Nb_3Cl_8$ in its HT and LT structures, showcasing the stacking and the change in distances between closest trimer centers across adjacent layers. (c) Closeup of the LT structure with the two relevant interlayer hoppings $t_{\mathrm{LT}}$ and $t'_{\mathrm{LT}}$ indicated. $U_{\mathrm{tr}}$ and $V_{\mathrm{tr}}$ represent the intra- and inter-trimer interactions considered in our calculations. (d) Energy level diagram of the $Nb_3Cl_8$ trimer. (e) DFT Band structure of LT bulk $Nb_3Cl_8$ with the Wannier bands superimposed. (f) Top view of the corresponding Wannier function for one of the trimers within an LT unit cell.

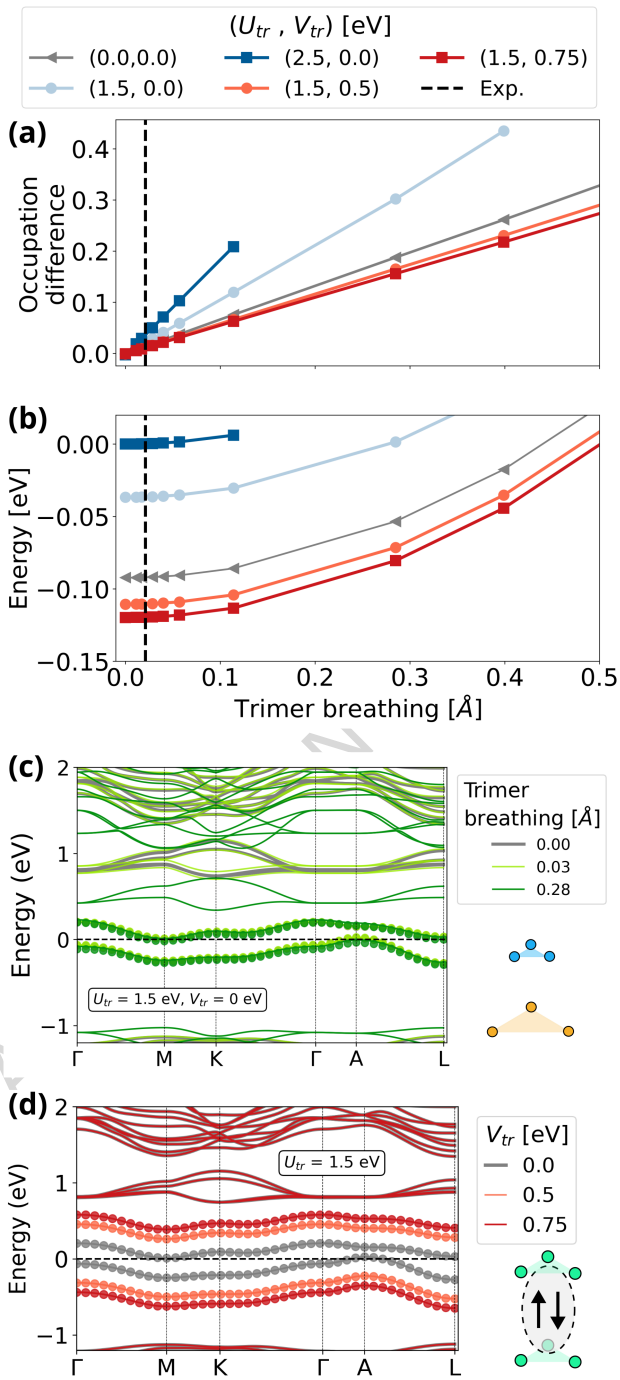



Figure 2: (a) Occupation difference between trimers and (b) total energy per unit cell as a function of the breathing mode for different values of $U_{\mathrm{tr}}$ and $V_{\mathrm{tr}}$. The vertical dashed line indicates the experimentally reported amplitude of the breathing mode from Ref. [28]. Band structure plots for (c) three breathing mode values at $(U_{\mathrm{tr}}, V_{\mathrm{tr}}) = (1.5, 0)$ eV and for (d) zero breathing mode ($R\bar{3}m$ structure) at three $V_{\mathrm{tr}}$ values for $U_{\mathrm{tr}} = 1.5$ eV. The trimer bands are highlighted with full circles.

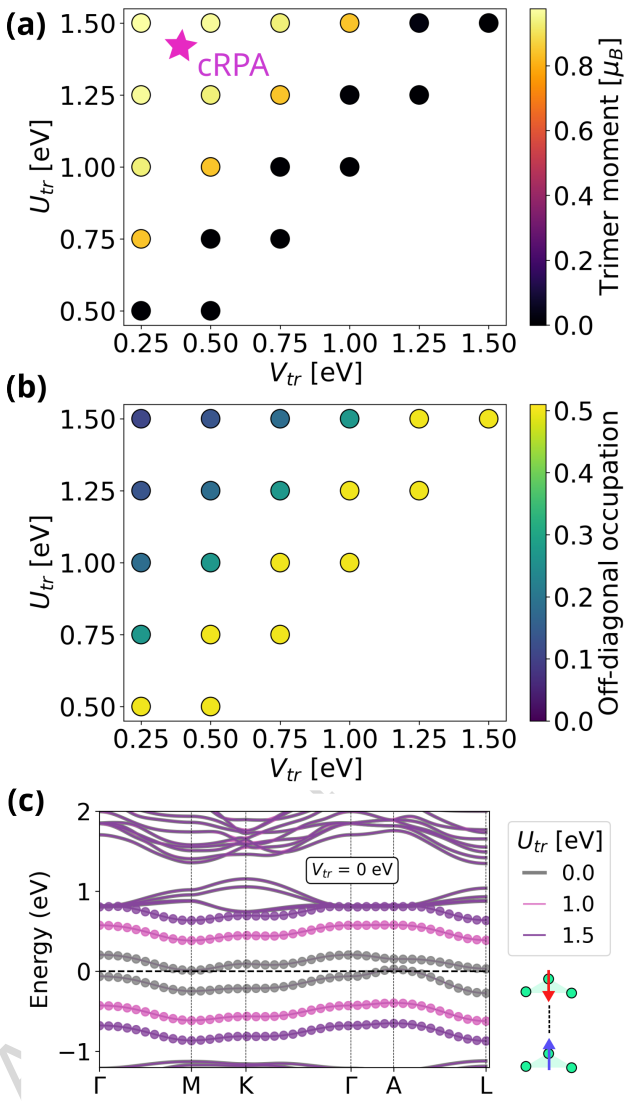



Figure 3: (a) Absolute value of the trimer moment and (b) intertrimer occupation as a function of $U_{\mathrm{tr}}$ and $V_{\mathrm{tr}}$. Star indicates the cRPA values. (c) Band structure within spin-polarized DFT+$U$+$V$ with antiferromagnetically aligned trimer magnetic moments for three $U_{\mathrm{tr}}$ values for $V_{\mathrm{tr}} = 0$. Bands corresponding to the trimer orbitals are highlighted with circles. All calculations are performed for the $R\bar{3}m$ structure (no trimer breathing mode).

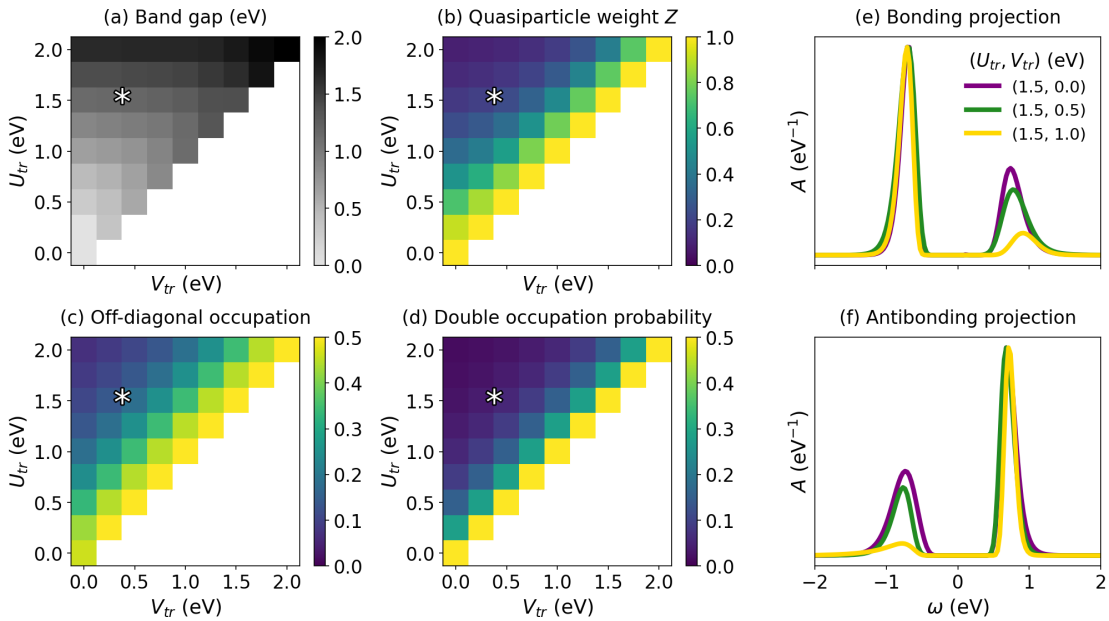



Figure 4: Observables of the $R\bar{3}m$ $Nb_3Cl_8$ cluster from DFT+DMFT as a function of $U_{\mathrm{tr}}$ and $V_{\mathrm{tr}}$. The cRPA values for $Nb_3Cl_8$ are shown with a star. (a) Band gap. (b) Quasiparticle weight, $Z$. (c) Off-diagonal occupation. (d) Double occupation probability. (e) Spectral function projected onto the bonding and (f) antibonding combination of the individual trimer orbitals across the ($U_{\mathrm{tr}}$, $V_{\mathrm{tr}}$) spectrum.

ARTICLE IN PRESS

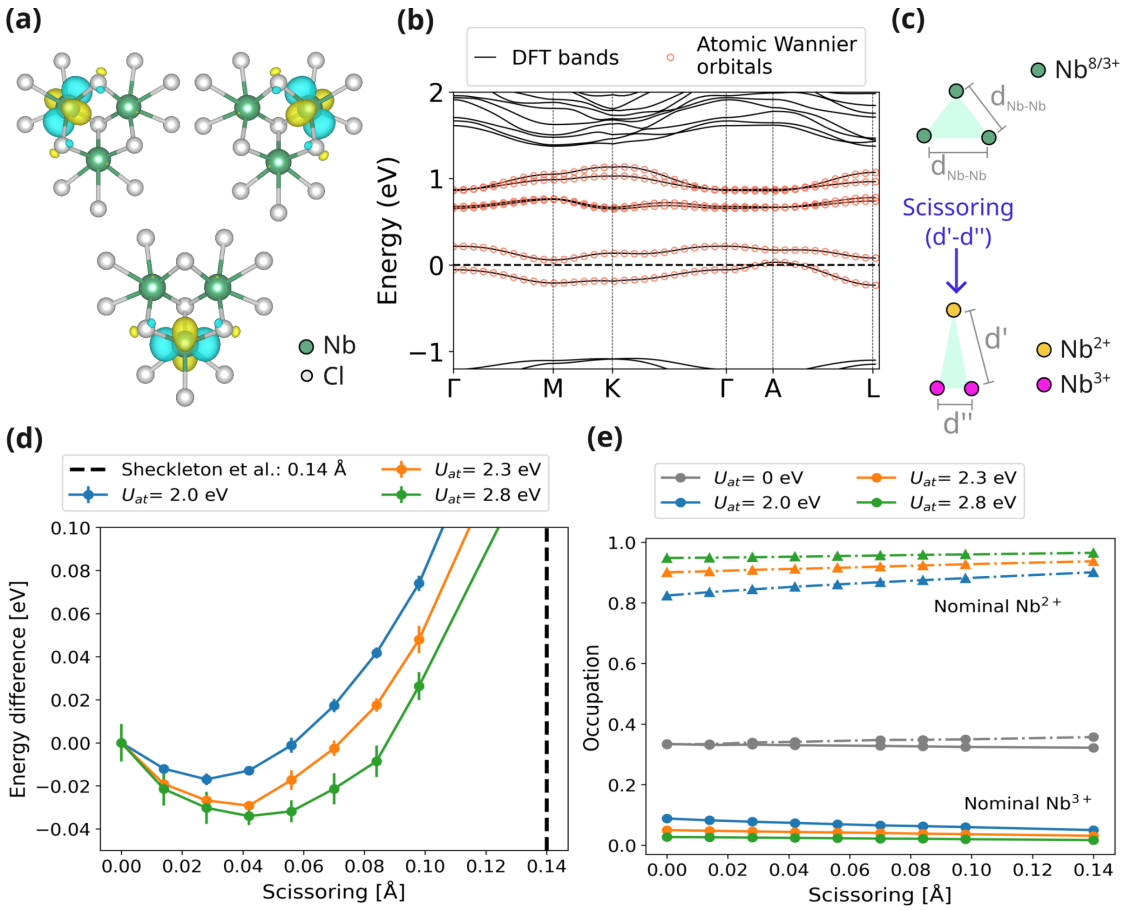



Figure 5: (a) Top view of the three atomic Wannier functions per trimer. (b) DFT band structure with the bands recalculated from the atomic Wannier model. (c) Schematic of the scissoring distortion within one trimer, connecting the $R\bar{3}m$ structure to the $C2/m$. (d) Energy difference per unit cell as a function of the scissoring amplitude. The black dashed line corresponds to the scissoring amplitude reported in Ref. [31]. (e) Occupation of the inequivalent Nb atoms inside one trimer. The solid lines correspond to the symmetry-equivalent nominal $Nb^{3+}$ sites, while the dash-dotted line corresponds to the nominal $Nb^{2+}$ site.

ARTICLE IN PRESS

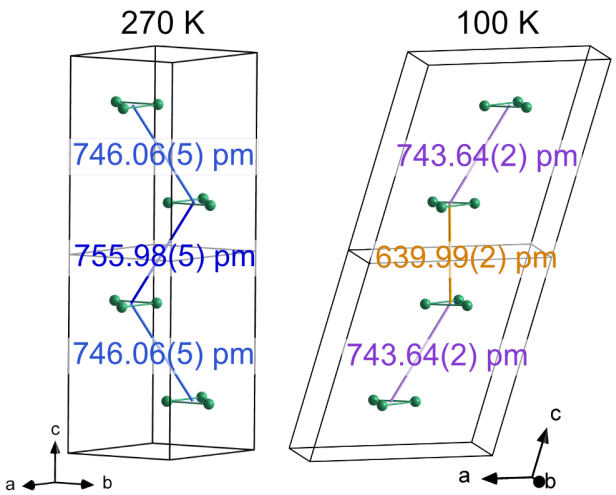



Figure 6: Stacking arrangement and distances of $Nb_3$ clusters (green triangles) in $Nb_3Br_{4-x}Cl_{4+x}$ as determined from single crystal X-ray diffraction data at 270 K (left) and 100 K (right). Chloride and bromide ions are omitted for clarity.

ARTICLE IN PRESS

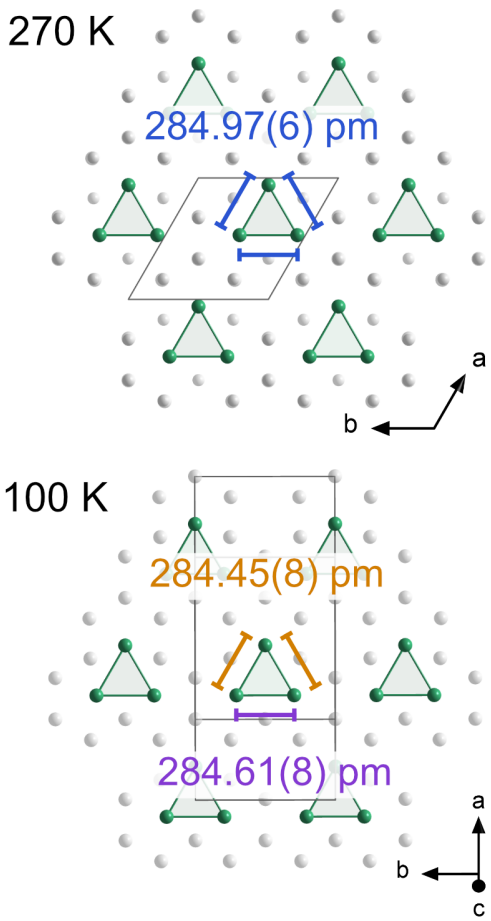



Figure 7: Nb–Nb distances within $Nb_3$ clusters in $Nb_3Br_{4-x}Cl_{4+x}$ as determined from single crystal X-ray diffraction data at 270 K (top) and 100 K (bottom). Niobium atoms are depicted in green, chloride and bromide ions are gray. The unit cell vectors are shown as grey lines.

ARTICLE IN PRESS

**Table 1: Selected crystallographic data of $Nb_3Br_{4-x}Cl_{4+x}$ above and below the transition temperature.**

| Formula* | $Nb_3Br_{3.7}Cl_{4.3}$ | $Nb_3Br_{3.8}Cl_{4.2}$ |
|---|---|---|
| CCDC number | 2364410 | 2365009 |
| Temperature | 270.0(1) K | 100.0(1) K |
| Crystal system | trigonal | monoclinic |
| Space group | $P\bar{3}m$ | $C2/m$ |
| Wavelength | 154.184 pm | 71.037 pm |
| Radiation type | Cu-$K_\alpha$ | Mo-$K_\alpha$ |
| Residual factor ($R_1$) | 0.0350 | 0.0350 |
| Residual factor ($wR_2$) | 0.0903 | 0.0909 |

*The composition variation is within the synthesis and refinement error margin, and is considered as $Nb_3Br_4Cl_4$.

ARTICLE IN PRESS

ARTICLE IN PRESS

**Table 2: Direct and indirect optical band gaps for $Nb_3Cl_8$ and $Nb_3Br_4Cl_4$ at room temperature, determined by DRIFT Spectroscopy. (See SI [20], Supplementary Fig. 4 and Supplementary Fig. 5 for full optical spectra)**

| | | |
|---|---|---|
| $Nb_3Cl_8$ | direct | 0.510 eV |
| | indirect | 0.344 eV |
| $Nb_3Br_4Cl_4$ | direct | 0.537 eV |
| | indirect | 0.311 eV |

ARTICLE IN PRESS